Evaluation of SOFC Anode Polarization Simulation using Three-Dimensional Microstructures Reconstructed by FIB Tomography

Daisuke Kanno[a, c], Naoki Shikazono[b]*, Norikazu Takagi[a, d], Katsuhisa Matsuzaki[a, e] and Nobuhide Kasagi[a]

[a] Department of Mechanical Engineering, The University of Tokyo, Hongo 7-3-1, Bunkyo-ku, Tokyo 113-8656, Japan

[b] Institute of Industrial Science, The University of Tokyo, Komaba 4-6-1, Meguro-ku, Tokyo 153-8505, Japan

*Corresponding author. Tel.: +81-3-5452-6776; FAX: +81-3-5452-6776

E-mail address: shika@iis.u-tokyo.ac.jp

Current affiliations

[c] Toyota Motor Corporation

1, Toyota-cho, Toyota, Aichi 471-8571, Japan

[d] Toshiba Corporation Power Systems Company,

2-4, Suehiro-Cho, Tsurumi-Ku, Yokohama 230-0045, Japan

[e] Tokyo Electric Power Company, Fukushima Daiichi Nuclear Power Station,

22 Kitahara, Ottozawa, Ohkuma-machi, Futaba-gun, Fukushima 979-1301, Japan

Abstract

In order to evaluate the numerical simulation method for solid oxide fuel cell anode polarization, three-dimensional lattice Boltzmann method simulation is carried out using Ni-YSZ microstructures reconstructed by a focused ion beam scanning electron microscope. The effects of reconstructed sample volume size on the three phase boundary length, tortuosity factors and overpotential are first investigated. The YSZ tortuosity factor has remained nearly unchanged when the cross-sectional area exceeds approximately 200 μm^2, whilst the pore tortuosity factor is almost independent of the sample volume size. On the other hand, the Ni tortuosity shows very large variation regardless of the sample volume size. The overpotential predicted with the largest volume size sample is slightly larger than those of smaller volume samples. Two exchange current models based on patterned electrodes are assessed presently. Both models give weaker dependence on the steam concentration than the experimental data. From the predicted three-dimensional current stream lines, it is found that the mirrored computational structure gives a thinner reactive layer because of the factitious connection of Ni phase. Thus, it is recommended to use larger volume size samples which can cover whole reactive thickness when discussing the local potential and flux distributions.

Key words: Solid oxide fuel cell, Anode, Microstructure, Numerical simulation, Polarization

1. Introduction

Solid oxide fuel cell (SOFC) is one of the most promising energy conversion devices, because of its high efficiency and fuel flexibility [1]. However, its cost reduction and long-term durability must be further improved before market introduction. Numerical simulation is expected to play an important role in improving the electrode, cell, stack and system designs. In order to construct a universal electrochemical model for simulating the transport characteristics of SOFC electrodes, it is indispensable to separate the effect of local electrochemistry at the three phase boundary (TPB) and that of microstructure morphology [2]. Because of the complex nature of the microstructure, patterned electrodes have been employed and analyzed to isolate local electrochemical reaction characteristics at well defined TPBs [3-8]. However, it is also reported that patterned electrodes are not stable and cannot maintain their initial microstructure during high temperature and humid operation [7, 8]. Thus, it is straightforward and practical to use real sintered electrodes to explore the local electrochemistry and morphology simultaneously and independently. For this purpose, it is indispensable to establish a method that can quantify three-dimensional electrode microstructures and simulate transports and reactions of mass species inside electrodes.

Recently, direct measurement of three-dimensional SOFC electrode microstructures has been reported using focused ion beam scanning electron microscopy (FIB-SEM) [9-14] and X-ray computed tomography (XCT) [15, 16]. Wilson et al. [9] reconstructed an anode microstructure by FIB-SEM, and compared its microscopic parameters such as three phase boundary (TPB) density with those from stereology. Iwai et al. [12] carefully quantified the TPB length and tortuosity factors of a Ni-YSZ anode reconstructed by FIB-SEM. However, the Ni and YSZ tortuosity factors showed large variations depending on the directions. It is reported that the sample volume size might not be large enough to obtain statistically converged values.

It is also very challenging to simulate electrode polarization in three dimensional microstructures. The recent progress in computational methods has made it possible to

conduct three-dimensional numerical simulation of SOFC electrodes [17-20]. These modeling works will provide local oxygen potential distribution inside the electrode, which affects local non-stoichiometry and physical properties of oxides such as ionic or electronic conductivities, lattice constants and Young's modulus, etc. [17]. Such information will be indispensable for further improving electrode performance and reliability. In addition, three dimensional modeling will make it possible to provide quantitative information for exchange current density per unit TPB length in a real electrode, which is one of the most important measures for electrode performance [18]. Suzue et al. [19] predicted anode polarization in a stochastically reconstructed three-dimensional Ni-YSZ microstructure using lattice Boltzmann method (LBM). Shikazono et al. [20] also used the LBM to predict anode polarization in a real Ni/YSZ microstructure reconstructed by FIB-SEM, and compared the numerical results with their own experimental data. In their simulation, the FIB-SEM structure was not large enough to cover the whole reactive region, so it was mirrored and repeated in the anode thickness direction to constitute the whole computational domain. However, it is still not clear how the sample volume size affects the numerical results, since only single reconstructed microstructure was tested. Verification of sample volume size dependence is indispensable for SOFC electrode microstructure quantification techniques. In addition, their prediction showed much weaker dependence on the water partial pressure than the experiment. Numerical models, especially the exchange current density model, need further validated to improve the range of their applicability.

In the present study, Ni-YSZ microstructures with different volume sizes are reconstructed by an FIB-SEM in order to verify the SOFC anode microstructure quantification schemes. The dependences of TPB density and tortuosity factors on the sample volume size are first evaluated. Then, the anode polarization is predicted by the LBM developed in the previous study [20]. Two exchange current models by de Bore [4] and Bieberle et al. [5] are assessed. Furthermore, the three-dimensional ionic and electronic current distributions obtained from different volume size structures are presented.

2. Experimental

2.1 Cell preparation and polarization experiment

An electrolyte supported button cell is used in this study. NiO-8YSZ anode (60:40 vol%, AGC Seimi Chemical Co., Ltd.) and $La_{0.8}Sr_{0.2}MnO_3$ chathode (AGC Seimi Chemical Co., Ltd.) were screen printed on the 0.5 mm thick 8YSZ electrolyte disk (Japan Fine Ceramics Co., Ltd.), and sintered at 1400℃ and 1150℃, respectively. Then, the anode was reduced at 800℃ for 1 hour. The SOFC was placed between two alumina tubes with glass seals. Platinum meshes were used as current collectors, which were mechanically pressed against the electrodes. The performance of SOFC was evaluated at different temperatures with humidified hydrogen as a fuel, and pure oxygen as an oxidant. I–V and electrochemical impedance spectroscopy measurements (frequency range $1–10^6$ Hz, AC signal strength 10mV) were conducted using Solartron frequency analyzer (1255B).

2.2 Microstructure Reconstruction

Dual-beam FIB-SEM (Carl Zeiss, NVision40) was used to obtain cross-sectional images of the anode. The details of microstructure reconstruction are described in Ref. [12]. In the present study, three samples with different volume sizes were prepared. The volume size of sample A is 22.3 μm × 8.56 μm × 12.7 μm (2.42×10^3 μm^3) in *x*, *y* and *z* directions, while those of samples B and C are 22.6 μm × 10.8 μm × 16.0 μm (3.91×10^3 μm^3) and 45.8 μm × 14.5 μm × 26.2 μm (1.74×10^4 μm^3), respectively. Sample C is the largest sample which covers whole electrode thickness (*x* direction). The cross-sectional resolutions are 37.2 nm/pixel for samples A and B, and 55.8 nm/pixel for sample C. The FIB milling pitch distances are 74.5, 61.7 and 74.7 nm for the three samples.

Three phases (pore, Ni, YSZ) in the cross-sectional images are distinguished by their brightness values. Epoxy infiltration resulted in very clear contrast of the pore phase [12]. The phase distinguished images are then aligned for three-dimensional reconstruction.

According to Ref. [20], spatial resolution of approximately 100 nm/voxel is recommended to obtain grid independent results for the LBM simulation. In addition, cubic voxels are required in the LBM mesh. Therefore, all the samples are rearranged in 124 nm cubic voxels in the present study. Reconstructed three dimensional structures of samples A, B, and C are shown in Fig. 1.

2.3 Quantification of 3-D parameters

Table 1 shows volume sizes and phase volume fractions of the three samples. The volume ratio of YSZ to the total solid phase (Ni + YSZ) for samples A, B, and C are 52.6, 55.0, and 56.5 vol%, respectively. These values are in relatively good accordance with the original YSZ material composition of 53.0 vol%.

Phase connectivity is defined as the ratio of connected voxels to the total voxels for each phase. Table 2 shows the connectivities from six boundaries. The connectivities are larger than 90% for all cases.

Table 3 shows total TPB lengths calculated from the centroid method [20]. It is confirmed that the variation of TPB lengths between the samples is relatively small.

Tortuosity factor is a measure for deterioration of diffusivity or conductivity in porous media. Physically, tortuosity factor represents 1) the increase of actual diffusion path lengths compared to the superficial thickness in the mean diffusion direction, and 2) the increase of diffusion flux according to the decrease of effective diffusive cross sectional area due to the inclination of the paths:

$$D_{\text{eff}} = \frac{\varepsilon_{\text{pore}}}{\tau_{\text{pore}}} D \tag{1}$$

$$\sigma_{\text{e}^-,\,\text{eff}} = \frac{\varepsilon_{\text{Ni}}}{\tau_{\text{Ni}}} \sigma_{\text{e}^-} \tag{2}$$

$$\sigma_{\text{O}^{2-},\text{eff}} = \frac{\varepsilon_{\text{YSZ}}}{\tau_{\text{YSZ}}} \sigma_{\text{O}^{2-}} \tag{3}$$

where D_{eff} and σ_{eff} are the effective diffusivity and conductivity, and ε is the volume fraction. Diffusion inside each phase is solved by the LBM, which will be described in detail in section 3. Figure 2 shows tortuosity factors of all samples plotted against cross-sectional areas normal to the direction of diffusion. The pore tortuosity factor is nearly constant regardless of cross sectional area. The YSZ tortuosity factor remains nearly unchanged when cross-sectional area exceeds 200 μm^2. This result indicates that pore and YSZ structures are nearly isotropic and homogeneous. On the other hand, Ni tortuosity shows very large variation even for the samples with large cross sectional areas. Even though the connectivity values of Ni phase are quite large as shown in Table 2, complex nature of Ni phase network results in very large variation of tortuosity values.

3. Numerical method for overpotential calculation

3.1 Governing equations

Assuming Ni and YSZ to be perfect electron and ion conductors, the diffusion equations of gas, electron and ion can be written as follows:

$$\nabla\left(D\nabla C_{\mathrm{H_2}}\right)=\frac{i_{\text{reac}}}{2F} \tag{4}$$

$$\nabla\left(\frac{\sigma_{\mathrm{e^-}}}{F}\nabla\mu_{\mathrm{e^-}}\right)=-i_{\text{reac}} \tag{5}$$

$$\nabla\left(\frac{\sigma_{\mathrm{O^{2-}}}}{2F}\nabla\mu_{\mathrm{O^{2-}}}\right)=i_{\text{reac}} \tag{6}$$

where i_{reac} is the reaction current. The right hand sides of Eqs. (4) to (6) are the source terms which represent local reactions at TPB. For the voxels which don't possess TPB at their edge, RHSs of Eqs. (4) to (6) are set to zero. In this study, dusty gas model (DGM) [21] is used for the gas diffusion model. Assuming constant total pressure in the electrode, DGM is written as follows:

$$\frac{N_i}{D_{i,k}} + \sum_{j=1,\, j\neq i}^{n} \frac{y_j N_i - y_i N_j}{D_{i,j}} = -\frac{1}{RT}\nabla p_i \tag{7}$$

Graham's law holds in constant total pressure, which gives:

$$\sum_{i=1}^{n} N_i \sqrt{M_i} = 0 \tag{8}$$

Gas diffusion coefficient is represented from Eqs. (7) and (8) as:

$$D = \left[\frac{1 - \alpha y_{\mathrm{H_2}}}{D_{\mathrm{H_2,\,H_2O}}} + \frac{1}{D_{\mathrm{H_2},k}} \right] \tag{9}$$

$$\alpha = 1 - \sqrt{\frac{M_{\mathrm{H_2}}}{M_{\mathrm{H_2O}}}} \tag{10}$$

Binary and Knudsen diffusivity are given by the following equations.

$$D_{\mathrm{H_2,H_2O}} = 0.018833 \sqrt{\frac{1}{M_{H_2}} + \frac{1}{M_{H_2O}}} \frac{T^{2/3}}{p\Omega_D \zeta^2_{H_2,H_2O}} \tag{11}$$

$$D_{\mathrm{H_2,k}} = \frac{2}{3} r_{\mathrm{mean}} \left(\frac{8RT}{\pi M_{\mathrm{H_2}}} \right)^{1/2} \tag{12}$$

The mean pore radius r_{mean} is calculated by the maximum sphere inscription method (MSI) [22]. The mean radii of samples A, B and C are r_{mean} = 422 nm, 416 nm and 462 nm, respectively.

Collision integral is given as:

$$\Omega_D = 1.1336 \left(\frac{kT}{\varepsilon} \right)^{-0.1814} \tag{13}$$

The intermolecular force constant $\zeta_{\mathrm{H2,\,H2O}}$ is taken as an arithmetic mean of ζ_{H2} and $\zeta_{\mathrm{H2O,}}$. ε is represented as geometric mean of $\varepsilon_{\mathrm{H2}}$ and $\varepsilon_{\mathrm{H2O}}$. The gas parameters are shown in Table 4.

The reaction current is given by the Butler-Volmer like equation as follows [19, 20]:

$$i_{\mathrm{reac}} = i_0 L_{\mathrm{TPB}} \left\{ \exp\left(\frac{2F}{RT} \eta_{\mathrm{act}} \right) - \exp\left(\frac{F}{RT} \eta_{\mathrm{act}} \right) \right\} \tag{14}$$

The lineal exchange current density i_0 is fitted from the patterned anode experiments of de Boer [4] and Bieberle et al. [5] as follows.

$$i_0 = 31.4 \times p_{\mathrm{H_2}}^{-0.03} p_{\mathrm{H_2O}}^{0.4} \exp\left(-\frac{1.52\times10^5}{RT}\right) \tag{15}$$

$$i_0 = 0.0013 \times p_{\mathrm{H_2}}^{0.11} p_{\mathrm{H_2O}}^{0.67} \exp\left(-\frac{0.849\times10^5}{RT}\right) \tag{16}$$

The values for the activation energy and the exponents of P_{H2} and P_{H2O} in Eq. (16) are taken from the zero overpotential data of Bieberle et al. [4], but the leading coefficient 0.0013 in Eq. (16) is chosen so that the predicted results fit best to the present experimental data at 10 mol% H_2O – 90 mol% H_2, 1073 K. The numerical conditions are listed in Table 5 [23, 24].

Local activation overpotential η_{act} in Eq. (14) is defined as follows [20]:

$$\eta_{\mathrm{act}} = -\frac{1}{2F}\left(2\tilde{\mu}_{\mathrm{e^-,lyte/WE}} - \tilde{\mu}_{\mathrm{O^{2-},lyte/WE}} + \Delta G^{\mathrm{o}} + RT\log\left(\frac{p_{\mathrm{H_2O}}}{p_{\mathrm{H_2}}}\right)\right) \tag{17}$$

In the LBM calculation, which will be described in detail in the following section, the electrochemical potential of electron $\tilde{\mu}_{\mathrm{e^-}}$ in the Ni phase and that of oxide ion $\tilde{\mu}_{\mathrm{O^{2-}}}$ in the YSZ phase are solved. In Eq. (17), $\tilde{\mu}_{\mathrm{e^-,lyte/WE}}$ and $\tilde{\mu}_{\mathrm{O^{2-},lyte/WE}}$ represent electron and oxide ion electrochemical potentials in Ni and YSZ at TPB. Local hydrogen and steam pressures at the vicinity of TPB are used in the last term of Eq. (17). In Eq. (17), the electron in the electrolyte side at the RE/electrolyte interface is assumed to be in equilibrium with that in the electrode side $\tilde{\mu}_{\mathrm{e^-,\,lyte/RE}}$. A local equilibrium condition $\tilde{\mu}_{\mathrm{O^{2-}}} = 2\tilde{\mu}_{\mathrm{e^-}} + \mu_{\mathrm{O}}$ is assumed in the electrolyte. In addition, at reference electrode RE, oxygen is assumed to be in equilibrium with the gaseous phase. All the variables in the RHS of Eq. (17) are defined at the voxels adjacent to the TPB segment, which are solved in the LBM calculation.

The total anode overpotential can be expressed as follows [20]:

$$\eta_{\text{anode}} = -\frac{1}{2F}\left(\tilde{\mu}_{\text{e}^-,\text{anode/CC}} - \tilde{\mu}_{\text{O}^{2-},\text{anode/lyte}} + \Delta G^{\text{o}} + RT\log\left(\frac{p_{\text{H}_2\text{O},\text{anode/CC}}}{p_{\text{H}_2,\text{anode/CC}}}\right)\right) \quad (18)$$

In Eq. (18), $\tilde{\mu}_{\text{e}^-,\text{anode/CC}}$ is the averaged electrochemical potential of electron at the anode current collector interface, and $\tilde{\mu}_{\text{O}^{2-},\text{anode/lyte}}$ is the averaged electrochemical potential of oxide ion at anode electrolyte interface. Averaged hydrogen and steam pressures at the anode and current collector interface are used in Eq. (18).

3.2 Numerical method

For samples A and B, three mirrored FIB-SEM structures are repeated in the anode thickness direction to secure sufficient electrode thickness. On the other hand, original single structure is used in the case of sample C which covers whole anode thickness. The electrolyte and current collector layers are added at both ends of the computational volume as shown in Fig. 3. The thicknesses of electrolyte and CC layers are 2.60 μm and 1.24 μm, respectively.

Equations (4) to (6) are solved by the LBM [19, 20]. D3Q6 (i=1-6) model is used in the present study. The LB equation with the LBGK model in the collision term is represented as follows:

$$f_i(\mathbf{x}+\mathbf{c}_i\Delta t, t+\Delta t) = f_i(\mathbf{x},t) - \frac{1}{t^*}\left[f_i(\mathbf{x},t) - f_i^{\text{eq}}(\mathbf{x},t)\right] + w_i\Delta t \quad (19)$$

In Eq. (19), f_i represents the density distribution function of gas, electron or ion with a velocity c_i in the i-th direction, and f_i^{eq} is the Maxwellian local equilibrium distribution,

$$f_i^{\text{eq}}(\mathbf{x},t) = \frac{1}{6}\sum_{i=1}^{6} f_i(\mathbf{x},t) \quad (20)$$

The relaxation time t^* can be written by diffusion coefficient, voxel size Δx and time step Δt as follows:

$$t^* = 0.5 + \frac{3D\Delta t}{\Delta x^2} \quad (21)$$

where D is given by Eq. (9). As can be seen from Eq. (9), the DGM diffusion coefficient is not uniform in space. Thus, relaxation time also varies according to the diffusion coefficient. The time step Δt is chosen so that relaxation time becomes $t^* = 0.99$ at the point where the diffusion coefficient D takes its maximum. The last term of Eq. (19) is a production term calculated from the reaction current, Eq. (14).

At the CC surface, constant gas composition (Dirichlet boundary) is assumed. Constant electronic and ionic current flux conditions (Neumann boundary) are imposed on CC and electrolyte boundaries, respectively. A zero gradient condition is assumed at other boundaries. At the phase interfaces inside the porous anode, a no-flux boundary condition is assumed by applying the halfway bounceback scheme with a second-order accuracy [25].

4. Results and Discussions

Overpotential calculations with the de Bore current density model are conducted in order to evaluate the effects of different sample volume sizes. Predicted anode overpotentials at 1073 K are shown in Fig. 4. For sample C, calculation is conducted only for the 3mol% H_2O - 97mol% H_2 case because of the computational cost. The predicted overpotential of the largest sample C is slightly larger than the smaller samples A and B, but the difference is less than 0.01 V. Thus, it can be said that small volume size results in underprediction of overpotential but its influence is relatively small.

Overpotential calculations are conducted in different steam partial pressures using sample A. Overpotential results with de Boer's exchange current density model (Eq. 15) are compared with the experimental data in Fig. 5. Figure 6 shows predicted results using Bieberle et al.'s exchange current density model (Eq. 16). In Fig. 5, prediction by de Boer's model shows weaker dependence on steam partial pressure than the experimental data. On the other hand, dependence on steam partial pressure is somewhat improved by the Bieberle et al.'s model in Fig. 6. This indicates that the exponent of P_{H2O} in Bieberle et al.'s exchange current density i_0 is preferred than the de Boer's model. However, still there's a

discrepancy between the prediction and experimental data. This discrepancy may be attributed not only to the exchange current density model but also to the gas diffusion model, since constant pressure is assumed in the present study. Validation of the gas diffusion model is now being carried out as an ongoing work.

Figure 7 shows overpotential predictions in sample A with different temperatures using de Boer's exchange current density model. The result indicates that the activation energy in de Boer's model somewhat overpredicts the temperature dependence. Figure 8 shows overpotential predictions with Bieberle et al.'s model. As can be seen from the figure, the temperature dependence agrees better with the experiment. This result supports the validity of Bieberle et al.'s activation energy.

Figure 9 shows ionic (red) and electronic (blue) current stream line distributions in samples A and C, for 3mol% H_2O - 97mol% H_2, i = 0.3 Acm^{-2} at 1073 K case. The total thicknesses including electrolyte and current collector layers are 41.8 μm and 49.5 μm for samples A and C, respectively. As can be seen from the figure, large portion of ionic current is exchanged to electronic current in the region close to the electrolyte. Electronic paths are more concentrated and reactive thickness is somewhat thinner for sample A than for sample C. This is considered to be due to the mirrored structures used in sample A, which resulted in factitious connections of the Ni network. In sample C, electron paths are more distributed and reactive TPBs, where ionic current is converted to electric current, distribute widely. As a result, ionic current must diffuse farther from the electrolyte to the current collector side through less conductive YSZ network. This might be the reason why sample C showed slightly larger overpotential than the smaller samples as shown in Fig. 4. It is thus recommended to use larger volume size samples which can cover whole reactive thickness when discussing the local potential and flux distributions.

5. Conclusions

Overpotentials of Ni/YSZ anode reconstructed by FIB-SEM are predicted to evaluate the effects of sample volume size and exchange current density models. YSZ tortuosity factor remains nearly unchanged when cross-sectional area exceeds approximately 200 μm^2, while pore tortuosity factor is almost independent of the sample volume size. However, Ni tortuosity shows very large variation regardless of sample volume size. Small volume size results in underprediction of the overpotential, but its influence is relatively small. Two exchange current models from the patterned electrode experiments of de Boer [4] and Bieberle et al. [5] are evaluated. The dependence on temperature with Bieberle et al's model agrees well with the experimental data. However, both models give weaker dependence on the steam concentration than the experimental data. Further studies on the H_2O partial pressure dependence of the exchange current density as well as the gas diffusion model should be required. From the visualized three-dimensional current stream lines, it is shown that effective reaction area becomes thinner for the mirrored computational structure because of the factitious connection of the Ni network. It is thus recommended to use larger volume size samples which can cover the whole reactive thickness when discussing the local potential and flux distributions.

Acknowledgments

This work was supported by the New Energy and Industrial Technology Development Organization (NEDO) under the Development of System and Elemental Technology on Solid Oxide Fuel Cell (SOFC) Project.

References

[1] S. C. Singhal and K. Kendall, *High Temperature Solid Oxide Fuel Cells*, Elsevier (2002).

[2] C. W. Tanner, K.-Z. Fung and A. V. Virkar, *J. Electrochem. Soc.*, **144** (1), 21-30 (1997).

[3] J. Mizusaki, H. Tagawa, T. Saito, K. Kamitani, T. Yamamura, K. Hirano, S. Ehara, T. Takagi, T. Hikita, M. Ippommatsu, S. Nakagawa and K Hashimoto, *J. Electrochem. Soc.*, **141** (8), 2129-2134 (1994).

[4] B. De Boer, Ph. D. Thesis, University of Twente, (1998).

[5] A. Bieberle, L. P. Meier and L. J. Gauckler, *J. Electrochem. Soc.*, **148** (6), A646-A656 (2001).

[6] A. Utz, H. Störmer, A. Leonide, A. Weber and E. Ivers-Tiffee, *J. Electrochem. Soc.*, 157 (6), B920-B930 (2010).

[7] A. Ehn, J. Hogh, M. Graczyk, K. Norrman, L. Montelius, M. Linne and M. Mogensen, *J. Electrochem. Soc.*, **157** (11), B1588-B1596 (2010).

[8] A. Utz, H. Störmer, D. Gerthsen, A. Weber and E. Ivers-Tiffee, *Solid State Ionics*, in press (2011).

[9] J. R. Wilson, W. Kobsiriphat, R. Mendoza, H.-Y. Chen, J.M. Hiller, D. J. Miller, K. Thornton, P.W. Voorhees, S. B. Adler and S. Barnett, *Nature Materials*, **5,** 541-544 (2006).

[10] D. Gostovic, J. R. Smith, D. P. Kundinger, K. S. Jones and E. D. Wachsman, *Electrochemical and Solid-State Letters*, **10** (12), B214-B217 (2007).

[11] P. R. Shearing, J. Golbert, R. J. Chater and N. P. Brandon, *Chem. Eng. Sci.*, **64**, 3928-3933 (2009).

[12] H. Iwai, N. Shikazono, T. Matsui, H. Teshima, M. Kishimoto, R. Kishida, D. Hayashi, K. Matsuzaki, D. Kanno, M. Saito, H. Muroyama, K. Eguchi, N. Kasagi and H. Yoshida, *J. Power Sources*, **195** (4), 955-961 (2010).

[13] S. Jorgensen, K. V. Hansen, R. Larsen and J. R. Bowen, *Ultramicroscopy*, **110**, 216-228 (2010).

[14] L. Holzer, B. Iwanschitz, Th. Hocker, B. Münch, M. Prestat, D. Wiedenmann, U. Vogt, P. Holtappels, J. Sfeir, A. Mai and Th. Graule, *J. Power Sources*, **196** (3), 1279-1294 (2011).

[15] J. R. Izzo, Jr., A.S. Joshi, K. N. Grew, W. K. S. Chiu, A. Tkachuk, S. H. Wang and W. Yun, *J. Electrochem. Soc.*, **155** (5), B504-B508 (2008).

[16] P. R. Shearing, J. Gelb, and N. P. Brandon, *J. Eur. Ceram. Soc.*, **30**, 1809-1814 (2010).

[17] K. Matsuzaki, N. Shikazono and Kasagi, N., *J. Power Sources*, 196 (6), 3073-3082 (2011).

[18] P. R. Shearing, Q, Cai, J. Golbert, V. Yufit, C. S. Adjiman and N. P. Brandon, *J. Power Sources*, **195**, 4804-4810 (2010).

[19] Y. Suzue, N. Shikazono and N. Kasagi, *J. Power Sources*, **184**, 52-59 (2008).

[20] N. Shikazono, D. Kanno, K. Matsuzaki, H. Teshima, S. Sumino and N. Kasagi, *J. Electrocchem. Soc.*, **157** (5), B665-B672 (2010).

[21] R. Krishna and J. A. Wesselingh, *Chem. Eng. Sci.*, **52**, 861-911 (1997).

[22] V. Novak, F. Stepanek, P. Koci, M. Marek and M. Kubicek, *Chem. Eng. Sci.*, **65** (7), 2352-2360 (2010).

[23] U. Anselmi-Tamburini, G. Chiodelli, M. Arimondi, F. Maglia, G. Spinolo and Z. A. Munir, *Solid State Ionics*, **110**, 35043 (1998).

[24] J. R. Ferguson, J. M. Flard and R. Herbin, *J.Power Sources*, **58**, 109-122 (1996).

[25] M. A. Gallivan, D. R. Noble, J. G. Georgiadis and R. O. Buckius, *Int. J. Numer. Mthods Fluids*, **25**, 249-263 (1997).

Figure captions

Fig. 1 Three-dimensional reconstructed anode structures: (a) sample A, (b) sample B, (c) sample C (Blue: YSZ, Green: Ni, Transparent: pore).

Fig. 2 Tortuosity factors against cross-sectional area.

Fig. 3 Computational domain example.

Fig. 4 Predicted overpotential results of different samples.

Fig. 5 Dependence of overpotential on steam concentration with de Boer's parameters.

Fig. 6 Dependence of overpotential on steam concentration with Bieberle's parameters.

Fig. 7 Dependence of overpotential on temperature with de Boer's parameters.

Fig. 8 Dependence of overpotential on temperature with Bieberle's parameters.

Fig. 9 Three-dimensional current stream line distributions (Red: ionic current, Blue: electronic current), (a) sample A and (b) sample C.

Tables

Table 1 Volume size and fractions of three phases.

Sample	Size $x \times y \times z$ [μm]	Pore [vol%]	YSZ [vol%]	Ni [vol%]	YSZ/(Ni+YSZ) [vol%]
A	22.3×8.56×12.7	48.7	27.0	24.3	52.6
B	22.6×10.8×16.0	46.9	29.2	23.9	55.0
C	45.8×14.5×26.2	49.8	28.4	21.8	56.5

Table 2 Connectivities of the phases: (a) Sample A, (b) sample B, (c) sample C.

(a)

	From $x = 0$	From $x = 22.3\mu m$	From $y = 0$	From $y = 8.56\mu m$	From $z=0$	From $z = 12.7\mu m$
Pore	99.82	99.81	99.81	99.87	99.82	99.82
YSZ	94.32	94.93	94.67	95.42	94.78	94.53
Ni	95.09	92.41	93.45	95.45	92.90	95.24

(b)

	From $x = 0$	From $x = 22.6\mu m$	From $y = 0$	From $y = 10.8\mu m$	From $z=0$	From $z = 16.0\mu m$
Pore	99.87	99.87	99.89	99.88	99.88	99.88
YSZ	97.01	97.01	97.47	96.99	96.99	97.17
Ni	93.77	94.29	94.77	94.30	94.30	93.77

(c)

	From $x = 0$	From $x = 45.8\mu m$	From $y = 0$	From $y = 14.5\mu m$	From $z=0$	From $z = 26.2\mu m$
Pore	99.82	99.82	99.82	99.84	99.82	99.82
YSZ	97.05	97.08	97.17	97.36	97.14	97.16
Ni	92.89	93.33	93.84	94.14	93.19	92.82

Table 3 Total TPB lengths of the samples.

Sample	Total TPB length [$\mu m/\mu m^3$]
A	2.11
B	1.92
C	2.05

Table 4 Gas properties.

Substance	M [g/mol]	ζ [Å]	ε/k [K]
H_2	2.016	2.93	37
H_2O	18.015	2.65	356

Table 5 Numerical Conditions.

Properties	Value
Total pressure p [Pa]	1.013×10^{5}
Electronic conductivity σ_{e^-} [Sm^{-1}] [22]	$3.27\times10^{6}-1065.3T$
Ionic conductivity $\sigma_{O^{2-}}$ [Sm^{-1}] [23]	$3.34\times10^{4}\exp(-10300/T)$
Gibbs free energy ΔG^{o} [$Jmol^{-1}$]	-177.99×10^{3}

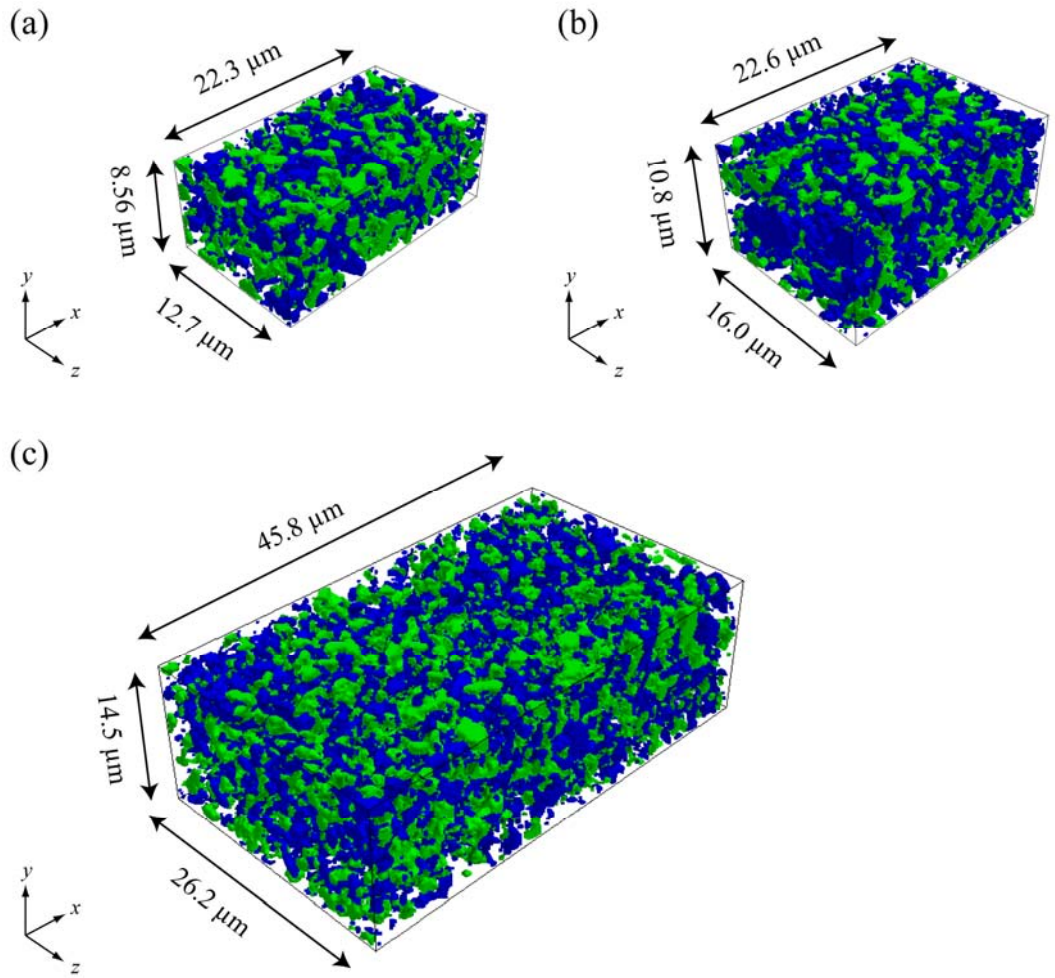

Fig. 1 Three-dimensional reconstructed anode structures: (a) sample A, (b) sample B, (c) sample C (Blue: YSZ, Green: Ni, Transparent: pore).

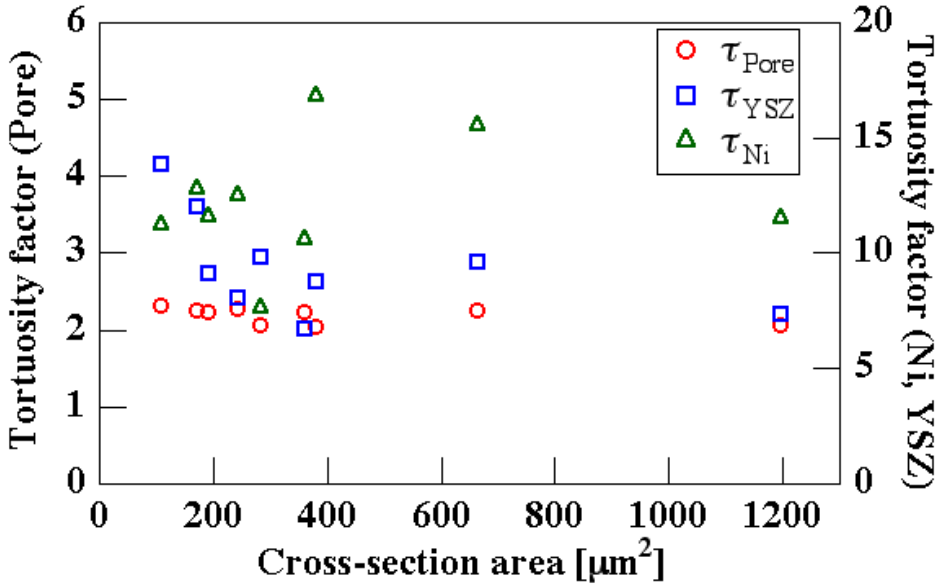

Fig. 2 Tortuosity factors against cross-sectional area.

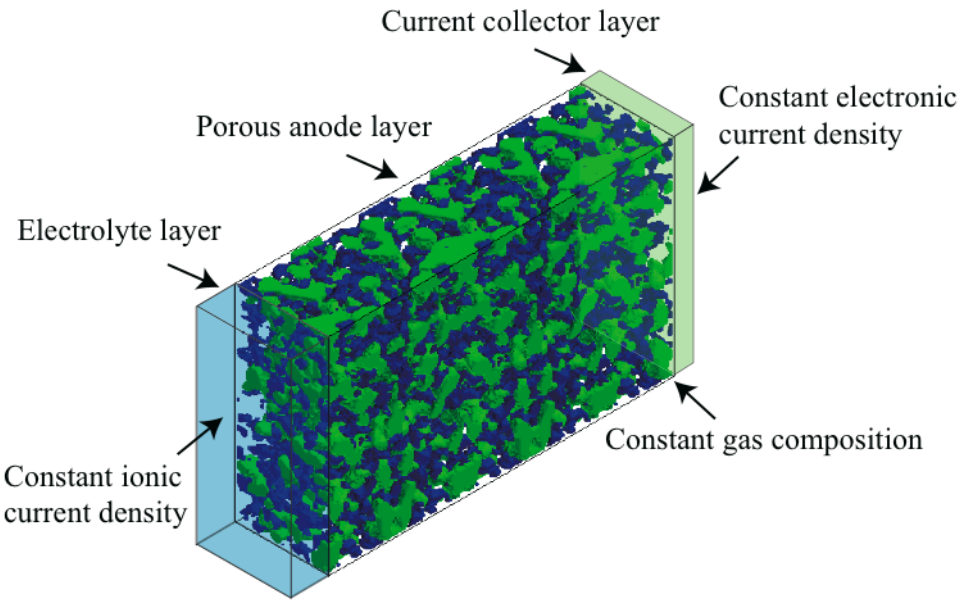

Fig. 3 Computational domain example.

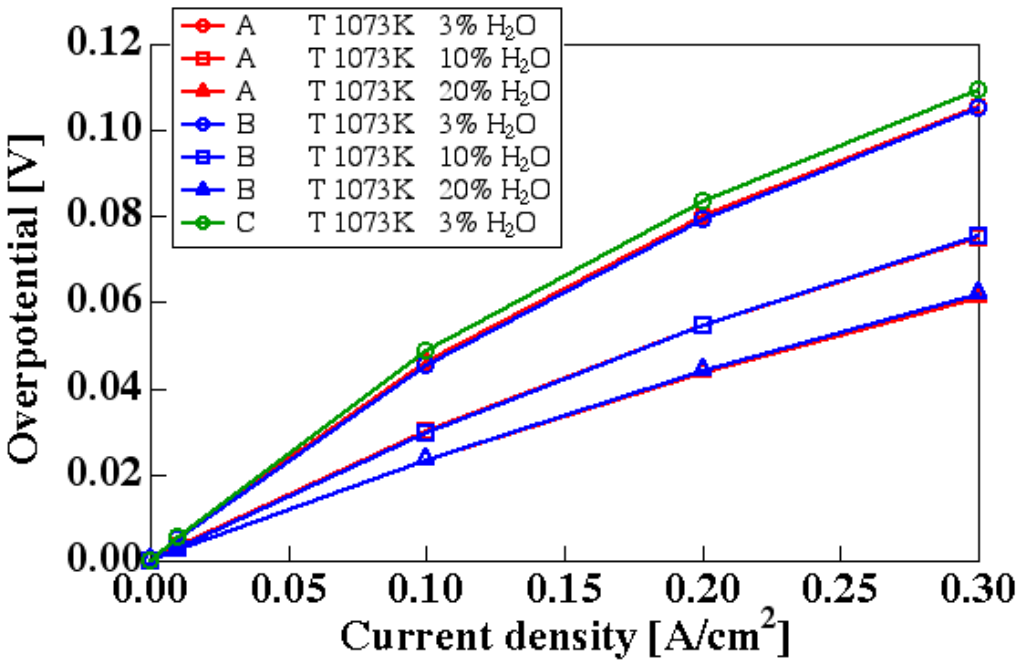

Fig. 4 Predicted overpotential results of different samples.

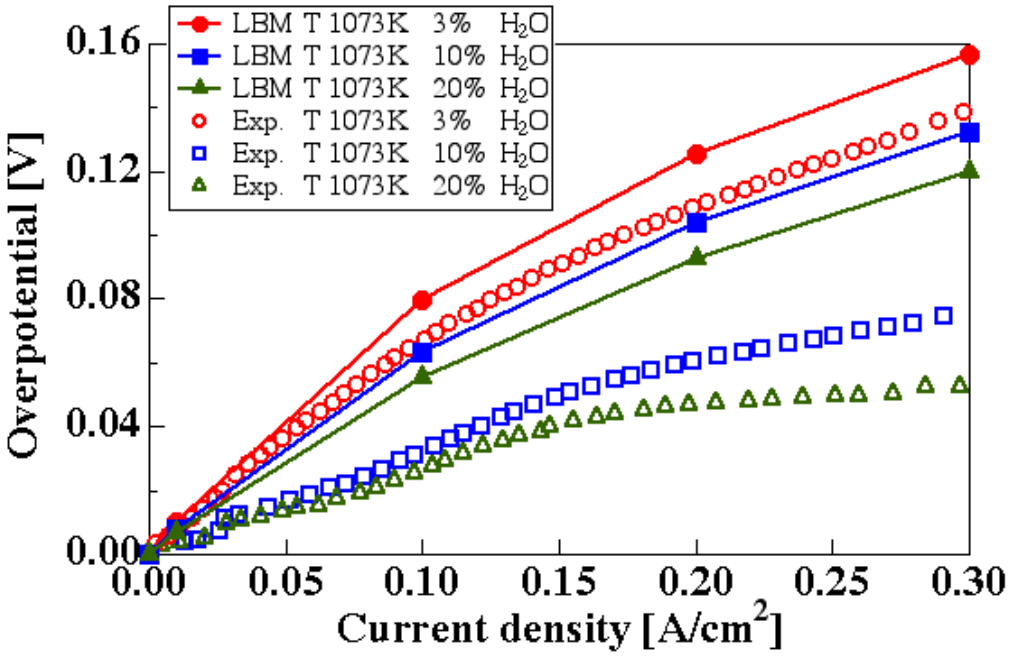

Fig. 5 Dependence of overpotential on steam concentration with de Boer's parameters.

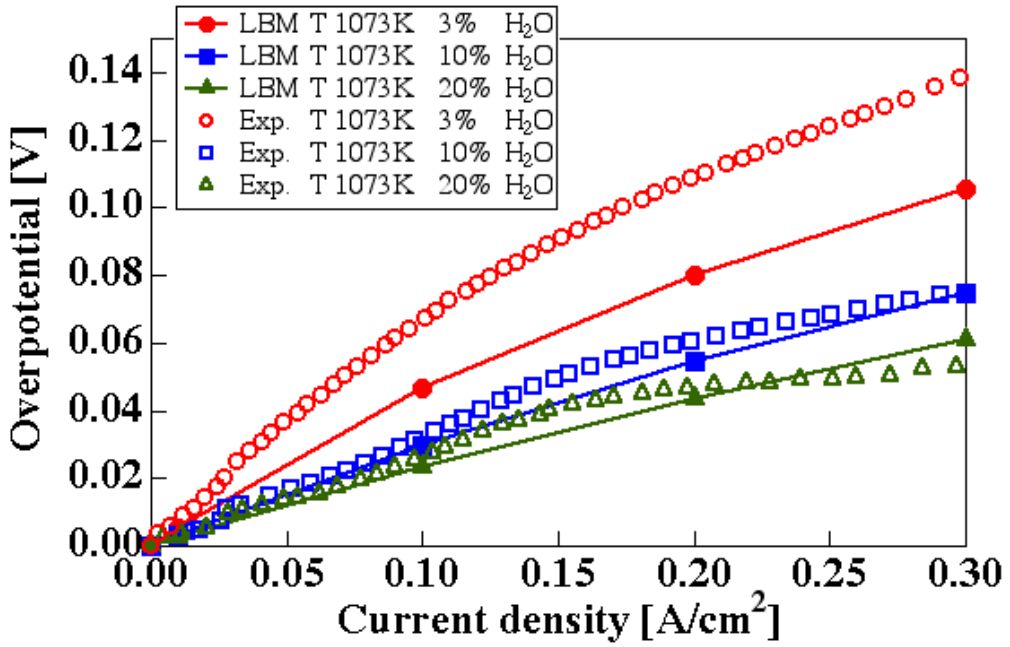

Fig. 6 Dependence of overpotential on steam concentration with Bieberle's parameters.

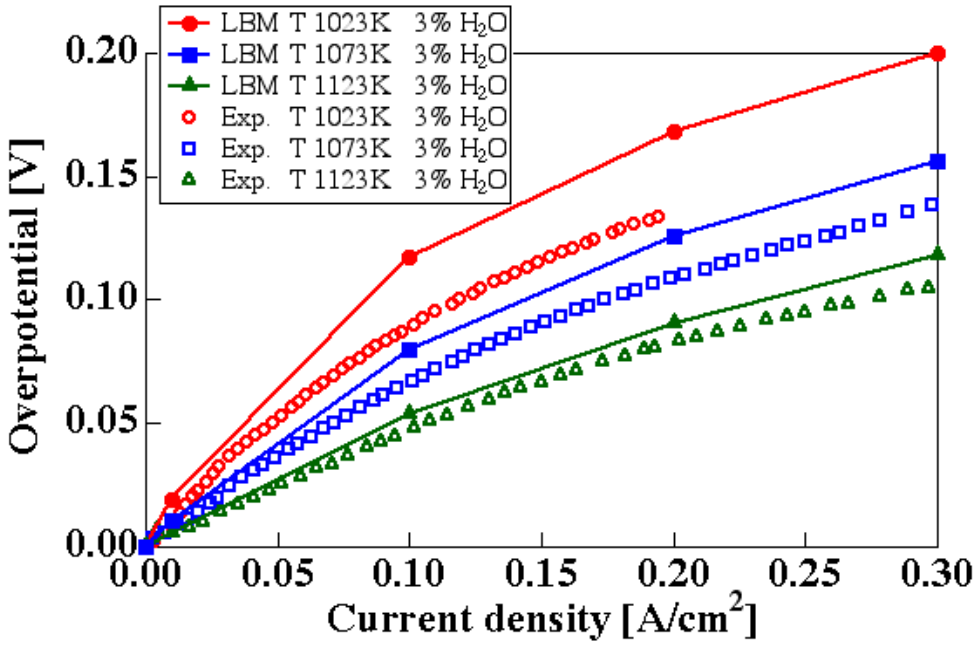

Fig. 7 Dependence of overpotential on temperature with de Boer's parameters.

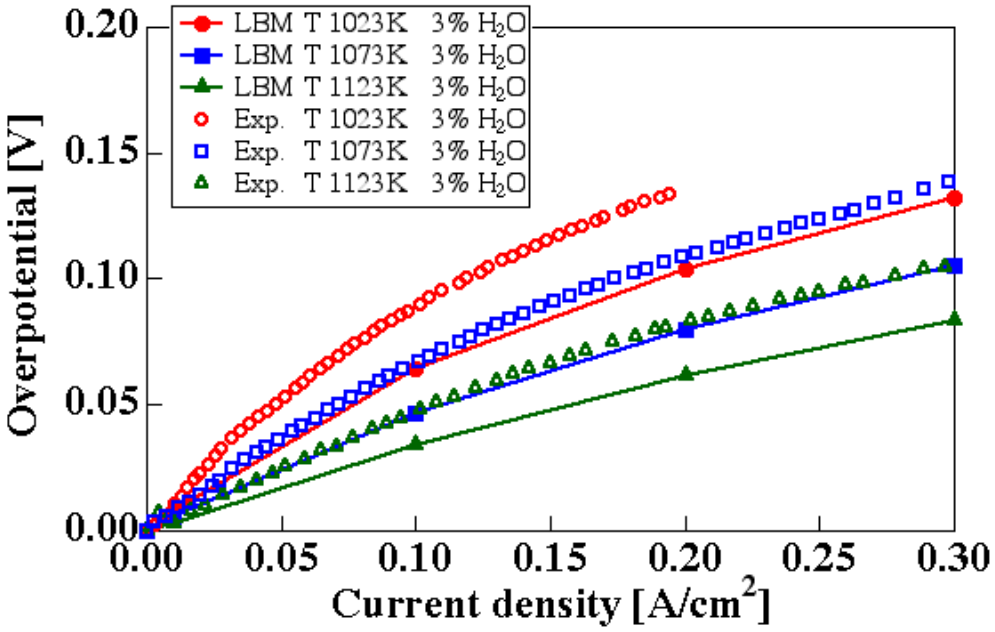

Fig. 8 Dependence of overpotential on temperature with Bieberle's parameters.

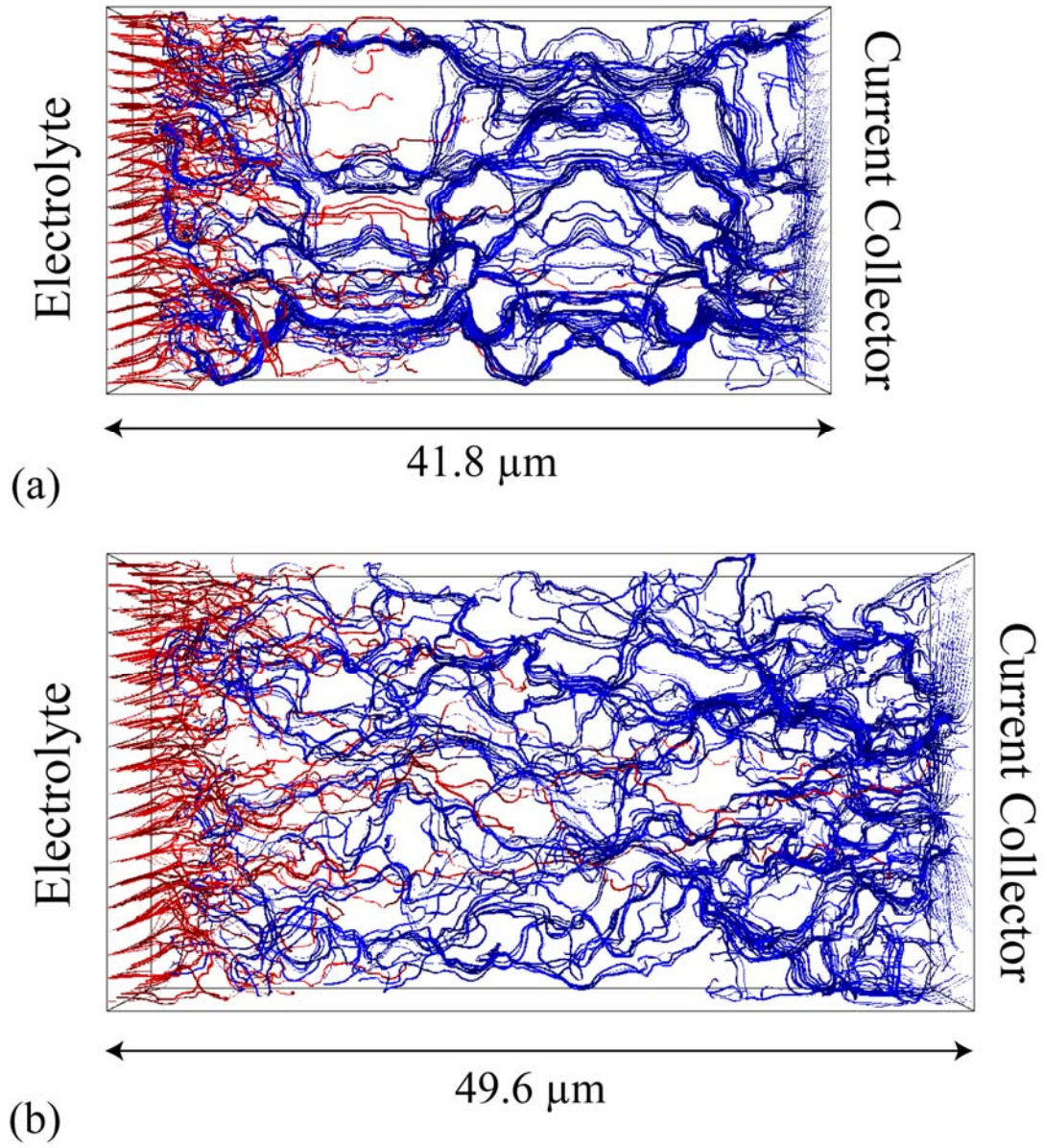

Fig. 9 Three-dimensional current stream line distributions (Red: ionic current, Blue: electronic current), (a) sample A and (b) sample C.